Research Article

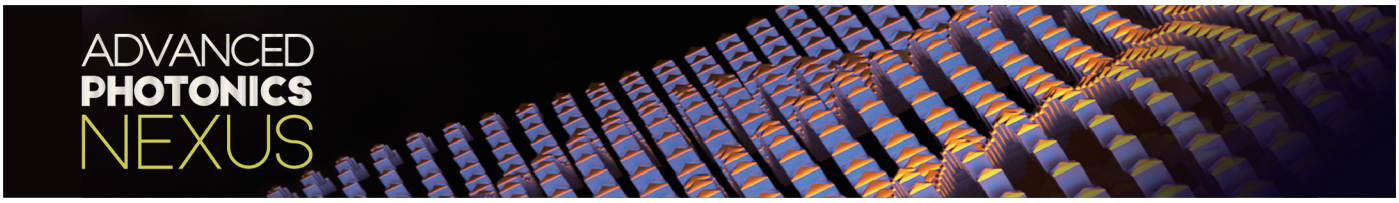

Enhanced characterization of depolarizing samples using indices of polarization purity and polarizance–reflection–transformation spaces

Dekui Li,[a,†] Ivan Montes,[b,†] Mónica Canabal-Carbia,[b] Irene Estévez,[b] Octavi Lopez-Coronado,[b] Zhongyi Guo,[a,*] Juan Campos,[b] and Ángel Lizana[b,*]
[a]Hefei University of Technology, School of Computer and Information, Hefei, China
[b]Autonomous University of Barcelona, Department of Physics, Optics Group, Bellaterra, Spain

Abstract. Depolarizing behavior is commonly observed in most natural samples. For this reason, optical tools measuring the differences in depolarization response among spatially separated structures are highly useful in a wide range of imaging applications for enhanced visualization of structures, target identification, etc. One commonly used tool for depolarizing discrimination is the so-called depolarizing spaces. In this article, we exploit the combined use of two depolarizing spaces, the indices of polarization purity (IPP) and polarizance–reflection–transformation (PRT) spaces, to improve the capability of optical systems to identify polarization–anisotropy depolarizers. The potential of these spaces to discriminate among different depolarizers is first studied from a series of simulations by incoherently adding diattenuations or retarders, with some control parameters emulating samples in nature. The simulated results demonstrate that the proposed methods are capable of increasing differences among depolarizers beyond other well-known techniques. Experimentally, validation is provided by conducting diverse phantom experiments of easy interpretation and mimicking the stated simulations. As a useful application of our approach, we developed a model able to retrieve intrinsic microscopic information of samples from macroscopic polarimetric measurements. The proposed methods enable non-invasive, straightforward, macroscopic characterization of depolarizing samples, and may be of interest for enhanced visualization of samples in multiple imaging scenarios.

Keywords: depolarizer; retarder; diattenuator; polarization space.

Received Jun. 12, 2024; revised manuscript received Nov. 9, 2024; accepted for publication Dec. 12, 2024; published online Jan. 9, 2025.

[DOI: 10.1117/1.APN.4.1.016009]

1 Introduction

Optical methods based on the fundamental characteristics of light are commonly applied in imaging applications in the search for structure visualization larger than that provided by standard intensity-based imaging systems. These methods exploit some features of light–matter interactions such as spectroscopic response, phase modification, and state of polarization transformation. In this last scenario, polarimetry, a well-established research field, provides a collection of methods and tools allowing the retrieval of polarization information of samples to foster visualization of some of their characteristics. The change in polarization information carried by light when interacting with samples is related to some inherent physical properties of the evaluated matter, such as dichroism, birefringence, and depolarization. By means of polarimetric techniques, these physical properties of samples can be obtained in a non-invasive and non-destructive way,[1] which significantly increases the possibility of identifying the samples that were unidentifiable.

On the one hand, polarimetric methods analyzing the dichroic or birefringent response of samples are well-established in the literature.[2] For instance, in the framework of bio-photonics, the

*Address all correspondence to Zhongyi Guo, guozhongyi@hfut.edu.cn; Ángel Lizana, angel.lizana@uab.es
†These authors contributed equally to this work.

birefringent characteristic of samples can be used to differentiate between healthy and cancerous tissues,[3] as well as to distinguish between elastic and collagen fibers in a rabbit aortic wall.[4] Besides, with the assistance of the diattenuation, brain regions can be distinguished from other neighboring tissues.[5]

On the other hand, methods studying depolarization have proved their major contribution to imaging applications. In fact, a widespread number of samples in nature present some kind of depolarizing behavior when interacting with polarized light, as is the case, for instance, of gases in the atmosphere, rough surfaces, plant samples, and animal tissues, among others. For this reason, imaging methods based on depolarizing analysis are crucial to enhance the visualization of samples consisting of multiple structures presenting different spatial depolarizing responses. In this framework, optical methods for depolarizing sample visualization are nowadays of importance in many areas, such as remote sensing,[6,7] astronomy,[8] plant imaging[9] and pathology detection in vegetal tissues,[10] three-dimensional (3D) graphics simulation,[11] self-driving cars integrated imaging sensors,[12,13] environmental studies,[14] material characterization for industry,[15–17] and biomedical applications,[18–20] for cancer detection in different human and animal tissues[21,22] and tissue recognition.[23] Furthermore, the investigations on generation,[24,25] transmission,[26–28] detection,[29,30] regulation,[31,32] and processing[33–39] of polarization information have deepened continuously.

Because of the above-stated interest in polarimetric (including depolarization) means in the analysis of samples, there is a continuous effort in developing polarimetric tools to foster polarimetric-based imaging methods state of art. In this framework, most advanced polarimetric methods are based on the experimental measurement, using polarimeters and the ulterior data analysis, of the Mueller matrix (MM) of samples. The MM is a 4×4 real matrix that encodes the polarimetric features of samples and is able to completely describe the polarimetric interaction between light and samples.[40] However, the 16 MM raw elements are complicated to interpret and cannot provide an intuitive link to the optical properties and structure of the samples described by MM. For this reason, a full field of study deals with MM decompositions and analysis,[41–46] deriving a series of physical observables that can be connected with specific polarimetric characteristics of samples. Importantly, these polarimetric observables have already provided their usefulness for imaging and automatic classification proposes.[47,48]

Besides, these polarimetric observables are interdependent and can form related polarization spaces, which further emphasize the visualization of depolarizers and data interpretation[40] and can be used as a criterion to implement pseudo-colored approaches for samples enhanced visualization.[10,19] Among these, some spaces are devised to specifically exploit depolarizing information of samples, the so-called depolarizing spaces, and a few of them have been proposed in the literature.[49] Generally, depolarizing spaces can be divided into two categories. In particular, the first category consists of the depolarizing spaces formed by the polarimetric observables that derive from the MM, such as components of purity space.[40] The second category consists of the depolarizing spaces formed by the polarimetric observables that are calculated from the eigenvalues of the H matrix of MM, such as λ space and $PI - P_\Delta$ space.[50,51] Note that the information represented by the depolarizing spaces from such two categories is completed for each by the other. Nowadays, depolarizing observables, belonging to the above-stated and other existing depolarizing spaces, are already being used in applications; for instance, observables of λ space are implemented for biological tissue identification,[19] and the indices of polarimetric purity (IPPs), or the polarization entropy (E_M) and depolarizing power (D_M), are employed to analyze dispersed systems.[52,53]

Importantly, from all those depolarizing spaces, the so-called IPP space[35] is especially interesting, as it maximizes the associated volume, which in turn leads to a larger distance between different depolarizers, this being useful, for instance, for sample discrimination and classificatory proposes. As an example, it has been already proved how the IPP space arises as an ideal framework for the study of biological samples.[19,20] Recently, a new depolarizing space was proposed in the literature, the polarizance–reflection–transformation (PRT) space,[54] with the idea of fostering some physical properties associated with depolarizers. It has been proven that the PRT space has significant superiority in distinguishing among different pure polarization systems. Moreover, for depolarizing samples, the polarimetric observable R in PRT space is able to identify the depolarization origin.

In this paper, we demonstrate how observables associated with depolarizing spaces can infer inherent information of sample unitary elements generating depolarization. To achieve this aim, we combine the information of two depolarizing spaces: the IPP and the PRT spaces. As discussed in this paper, the selection of these two spaces is not arbitrary; we chose them because their combined information led to a complete description of polarization–anisotropy depolarization present in samples. In particular, previous studies demonstrate that the IPP space shows its greater discriminatory capacity.[35,49] In this study, we use IPPs as a starting point because they have been described in the current state of the art as the most suitable space for depolarization in terms of volume (hence, for spatially separating depolarizers) as well as for distinguishing among different depolarizers. In addition, as demonstrated throughout this work, the PRT space has a greater discriminatory capacity than the IPP space for certain types of depolarizing samples, so we propose the combined use of these two spaces for an optimal description of depolarizing samples. Note that polarization–anisotropy depolarization relates to polarimetric anisotropies (dichroism and/or birefringence anisotropies) within inherent microscopic unitary elements in samples. Under this scenario, we show how the IPP–PRT spaces-based method here proposed can provide fundamental information on the structures in samples responsible for generating depolarization. Importantly, the proposed method obtains such relevant information from the macroscopic MM of samples, and thus, the sample description is obtained without the necessity of using microscopic optical systems. In addition, it can also be implemented non-invasively and in real time using an adequate polarimeter. In summary, in this work, we present the possibility of using depolarization spaces to obtain inherent physical characteristics of depolarizing samples via macroscopic measurements. To achieve this, we propose the combined use of IPP and PRT spaces, demonstrating that they provide an ideal framework for the description of anisotropic depolarizers

The outline of the present paper is as follows. In Sec. 2, we review the theoretical fundamentals required to describe the proposed method: the IPP (Sec. 2.1) and the PRT (Sec. 2.2) spaces. Afterward, in Sec. 3.1, we show how to combine the information of such spaces to understand the physical characteristics of depolarizing samples. To do so, we simulate a huge number of

polarization–anisotropy depolarizers by incoherently adding a series of pure elements (diattenuators and retarders) with some control parameters as the orientation or the dispersion of the elements in the summation, as well as their main values (diattenuation and retardance values). This simple model for simulated depolarizer generation tries to mimic scenarios found in real samples, as could be the case of vegetal (e.g., cell walls rich in cellulose, which is a dichroic organic compound) or animal tissues (e.g., rich in collagen fibers, which are birefringent compounds). Next, this collection of simulated depolarizers is represented in the IPP and PRT spaces to connect physical meaning with the raw contents of the sample MM. Later on, the discussion presented in Sec. 3.1 is experimentally validated in Sec. 3.2 by constructing depolarizers from experimentally measured, with a complete imaging polarimeter, and MMs of pure polarimetric elements (diattenuators and retarders) with different control parameters. An excellent agreement is obtained between simulations and experimental data, providing strong evidence of the proposed approach suitability. Then, in Sec. 3.3, we propose a practical application of the provided methods, by providing a new method, based on PRT space–associated observables, able to obtain inherent information of depolarizing units through correlation analysis between structural information and polarimetric observables. Finally, the main conclusions of the work are provided in Sec. 4, where we highlight the applicability of the method to readily infer information from samples without *a priori* knowledge and by means of a non-invasive and macroscopic way.

2 Materials and Methods

In this section, we provide a description of the two depolarizing spaces selected to implement the subsequent approach presented in Sec. 3. In particular, the IPP[55] and the PRT[54] spaces are detailed. We choose to use the IPP space as a framework for sample analysis as it has been proved that it is an ideal candidate for dealing with depolarizing samples. In addition, the information provided by the IPP space is complemented by the PRT space, as it provides, as will be proved in Sec. 3, complementary information of samples, the combined use of both spaces leading to a complete description of polarization–anisotropy depolarizing samples.

2.1 IPP Space and P_1P_2 Space

To describe the polarimetric characteristics of light and matter, the Stokes–MM formalism[16] is employed as our mathematical framework. In this framework, the state of polarization (SoP) of light is represented by a four-element vector called the Stokes vector, whereas the interaction between the light and samples can be represented by a 16-element real matrix called the MM with the following form:

$$\mathbf{M} = \begin{bmatrix} m_{00} & m_{01} & m_{02} & m_{03} \\ m_{10} & m_{11} & m_{12} & m_{13} \\ m_{20} & m_{21} & m_{22} & m_{23} \\ m_{30} & m_{31} & m_{32} & m_{33} \end{bmatrix}. \tag{1}$$

In theory, MM elements contain information on all the polarimetric characteristics related to the physical properties of the samples. Furthermore, except for some polarimetric characteristics intuitively expressed by elements in MMs, such as diattenuation and polarizance that can be directly calculated from MM elements, other useful polarimetric characteristics are codified within the MM elements without direct identification. Therefore, it can be useful to deeply analyze MMs for extracting complete polarimetric characteristics of the sample, such as retardance or depolarizing properties. To do so, several approaches for the decomposition of MMs have been proposed.[56,57] For instance, parallel decomposition focuses on the study of the depolarizing properties of samples, this decomposition considers a depolarized MM as a convex sum of up to four nondepolarizing MM,[16] which means that a depolarizing sample can be considered as an incoherent addition of non-depolarization samples whose weights equal the eigenvalues of the covariance matrix $\mathbf{H}$ of MMs, represented as λ_0, λ_1, λ_2, and λ_3.[40]

Based on such coefficients, there are several eigenvalue-based polarimetric parameters derived to measure the depolarization of given samples. In particular, the so-called IPP parameters[35] describe the polarimetric randomness introduced by samples to incident light, and they have demonstrated their potential for discrimination and contrast enhancement in tissue samples, showing a better performance than other referential depolarization metrics such as the overall depolarization index (P_Δ) and other eigenvalue-based metrics.[49] The IPP consists of three polarimetric indices, namely, P_1, P_2, and P_3, respectively defined as

$$P_1 = (\lambda_0 - \lambda_1)/\mathrm{tr}\mathbf{H}, \tag{2}$$

$$P_2 = [(\lambda_0 - \lambda_2) + (\lambda_1 - \lambda_2)]/\mathrm{tr}\mathbf{H}, \tag{3}$$

$$P_3 = [(\lambda_0 - \lambda_3) + (\lambda_1 - \lambda_3) + (\lambda_2 - \lambda_3)]/\mathrm{tr}\mathbf{H}. \tag{4}$$

Note that all of them range from 0 to 1.

By IPP, the overall depolarization index can be calculated as

$$P^2_{\Delta(\mathrm{Purity})} = 2P_1^2/3 + 2P_2^2/9 + P_3^2/9. \tag{5}$$

Due to the restrictions on the coefficients ($\lambda_0 \geq \lambda_1 \geq \lambda_2 \geq \lambda_3 \geq 0$ and $\lambda_0 + \lambda_1 + \lambda_2 + \lambda_3 = 1$), the values of IPP follow the inequalities

$$0 \leq P_1 \leq P_2 \leq P_3 \leq 1, \tag{6}$$

where $P_1 = P_2 = P_3 = 1$ represents pure nondepolarizing systems, and $P_1 = P_2 = P_3 = 0$ corresponds to ideal depolarizers. Furthermore, IPP can relate to well-known depolarizers. Importantly, depolarization is produced by complex light–matter interaction processes, but in general, it is regarded as resulting from the randomness induced in the polarization of the incident SoPs when interacting with the samples. Recently, it has been reported that the IPP parameters provide information on two different sources of depolarization induced by samples.[55] In this sense, P_1 and P_2 parameters have information on polarization–anisotropy depolarization, where the depolarization is originated by polarimetric anisotropies presenting in the elemental units comprising the samples (such as retarder and diattenuator units). In contrast, P_3 provides the polarization–isotropy depolarization content of samples (originated by polarization–isotropy structures leading to light scattering processes), with limit cases of $P_3 = 1$ for samples without showing polarization–isotropy depolarization behavior and $P_3 = 0$ for samples whose depolarizing response is fully governed by polarization–isotropy depolarization. Note that polarization–

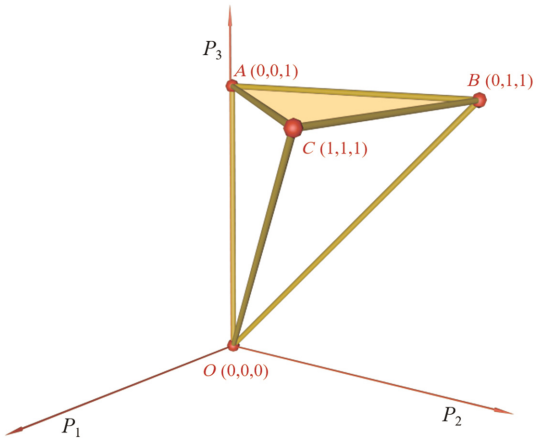

Fig. 1 IPP space representation. The P_1P_2 ($P_3 = 1$) surface, where the pure polarization–anisotropy depolarizers are represented, is shaded in the picture.

isotropy depolarization contribution describes the fraction of polarized light fully depolarized by samples (independently of the input state of polarization), in which any polarimetric sample feature is lost.

What is more, the IPPs are also useful for implementing a physical geometrical space, namely, IPP space, based on the dependence among P_1, P_2, and P_3.[40] As shown in Fig. 1, the IPP space is a 3D geometrical space with three coordinate axes as P_1, P_2, and P_3 along with the X, Y, and Z directions, respectively.

The IPP space contains all the physically realizable depolarizers where each point represents a depolarizer with unique depolarization characteristics. Generally, as closer the depolarizer to point O in Fig. 1, the lower the value of P_3 and the larger the polarization–isotropy depolarization content. In turn, the shaded surface in Fig. 1, corresponding to $P_3 = 1$, includes all possible pure polarization–anisotropy depolarizers. As limit cases, non-depolarizing samples are characterized by $P_1 = P_2 = P_3 = 1$ (point C). Conversely, samples with $P_1 = P_2 = P_3 = 0$ are regarded as ideal depolarizers, and they are located at point O. Last but not least, as discussed above, IPP space is a suitable tool to distinguish polarization–anisotropy depolarizers from polarization–isotropy depolarizers and to estimate the fraction of each depolarizing origin in arbitrary depolarizers. However, it is important to emphasize here, as it will be important in further sections, that the IPP space cannot distinguish among different typologies of polarization–anisotropy depolarizers, for instance, among those originated by diattenuator or retarder unitary elements.

2.2 PRT Space

In addition to IPP observables constituting the IPP space, there are several important polarimetric observables with clear physical meaning derived from MMs. In this subsection, we focus on reviewing those observables constituting the so-called PRT space.[54] We choose to include this space in the present study because, as it will be proved in this paper, it is a perfect space to complement the information of the IPP space in terms of depolarizing sample characterization. In the following, we derive the observables associated with the PRT space.

The MM illustrated in Eq. (1) can be normalized by m_{00} and expressed in its block form as[16]

$$\hat{\mathbf{M}} = \begin{bmatrix} 1 & \mathbf{D}^{\mathrm{T}} \\ \mathbf{P} & \mathbf{m} \end{bmatrix}, \tag{7}$$

where $[.]^{\mathrm{T}}$ refers to a transpose of a matrix, $\mathbf{P}$ is the polarizance vector, $\mathbf{D}$ is the diattenuation vector, and $\mathbf{m}$ is a submatrix of the $\hat{\mathbf{M}}$. Besides, according to $\mathbf{D}$, $\mathbf{P}$, and $\mathbf{m}$, the scalar diattenuation (D), polarizance (P), and degree of spherical purity (P_S) can be derived.[16] In addition, regarding each element in the $\mathbf{m}$ individually, it demonstrated the relation between Stokes elements of the incident and emergent beams. For instance, the diagonal elements (m_{11}, m_{22}, and m_{33}) intuitively characterize the direct reflectivity or transmittance of the Stokes elements (Q, U, and V) for the reflection or transmission scenario respectively (hereafter, the reflectivity is used). Thus, they are extracted to measure the direct reflectivity of different Stokes elements, and then, the overall reflectivity of Stokes elements is defined as[54]

$$R = \sqrt{\sum_{i=1}^{3} m_{ii}^2}/\sqrt{3}. \tag{8}$$

Besides, the rest elements ($m_{12}, m_{13}, m_{21}, m_{23}, m_{31}$, and m_{32}) characterize the mutual transformations among the Stokes elements (Q, U, and V) from the incident beam to the emergent beam. The overall transformation among the Stokes elements is defined as[54]

$$T = \sqrt{m_{12}^2 + m_{13}^2 + m_{21}^2 + m_{23}^2 + m_{31}^2 + m_{32}^2}/\sqrt{3}. \tag{9}$$

Because the elements employed to define R and T originate from $\mathbf{m}$, both R and T have contributions from the birefringent properties of the sample. Besides, the polarimetric P_P derived from $\mathbf{D}$ and $\mathbf{P}$ is able to characterize the dichroism of samples (without retardance contribution)

$$P_P = \sqrt{m_{10}^2 + m_{20}^2 + m_{30}^2 + m_{01}^2 + m_{02}^2 + m_{03}^2}/\sqrt{2}. \tag{10}$$

These three polarimetric observables P_P, R, and T contain all elements of MM except the normalized m_{00}, they being able to represent all information of systems. In particular, P_P, R, and T can represent dichroism, reflectivity, and transformation of Stokes elements, respectively. P_S can be calculated from R and T, leading the combination of R and T to represent the retardance of systems. Furthermore, the combination of P_P with R and T can obtain P_Δ representing the depolarization of systems. More importantly, based on such polarimetric indices, a novel 3D polarimetric representation with clear physical interpretation, named PRT space, is constructed, where R, T, and P_P variables correspond to X, Y, and Z axes, respectively, as seen in Fig. 2.

Like other depolarizing spaces described in the literature, each location in the PRT space represents the characteristics of different depolarizers. Moreover, due to the physical meaning of the PRT-based observables, the space, surfaces, and even lines in the PRT space can be associated with different polarimetric sample classes. For instance, the points on the surface

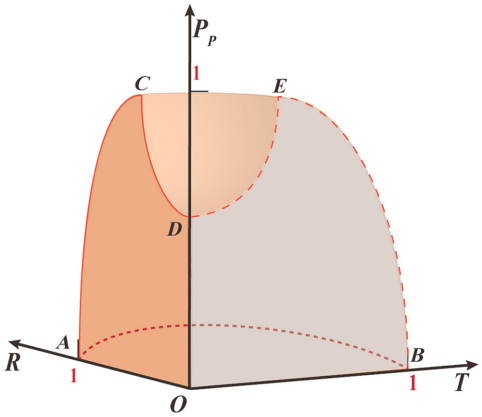

Fig. 2 Solvable domain of the PRT space.

ABCE represent non-depolarizing pure systems. Conversely, point *O* represents the ideal depolarizers that always fully depolarize light, independently of the input state of polarization. Except for the points at the locations above described, the rest of the points in the PRT space represent non-ideal depolarizing systems, i.e., depolarizers that introduce certain depolarization at the exit light beam but the light is not fully depolarized for some input SoP cases.

As above stated, any depolarizer can be considered a linear combination of pure non-depolarizing systems, such as diattenuators, retarders, or combinations of them.[45] In the PRT space, the depolarization originates from the combination of the decomposed pure systems with various polarizance, reflection, and transformation characteristics for the Stoke elements, which induces polarization randomness to the incident beam.

Last but not least, according to the definition of the depolarization index P_Δ,[46] the PRT can be defined from the P_P, R, and T as

$$P^2_{\Delta(\mathrm{PRT})} = 2P_P^2/3 + R^2 + T^2. \tag{11}$$

As a consequence, we can establish a connection between IPP and PRT spaces through the P_Δ metric by comparing Eqs. (5) and (11):

$$2P_1^2/3 + 2P_2^2/9 + P_3^2/9 = 2P_P^2/3 + R^2 + T^2. \tag{12}$$

In summary, both IPP and PRT spaces provide information on depolarizers, but the provided information, even if being both connected with the overall depolarization of samples (as provided by the connection of both spaces with P_Δ), is organized in different ways, leading to different description of the system characteristics. On the one hand, the IPP measures the magnitude of randomness induced by samples to incident beams, regardless of the specific polarization characteristics, and they are able to discriminate between polarization–isotropy and polarization–anisotropy depolarizers. On the other hand, the PRT space highlights the physical characteristics of the sample involved in the depolarizing process and, in particular, the overall polarizance, reflectivity, and transformation between the input and exiting Stokes elements. In other words, the IPP and PRT spaces describe the depolarization of samples from different physical (and complementary) perspectives.

3 Results and Discussion

3.1 Characterization of Different Depolarizers

In this section, we present a collection of simulations to provide the potential of the combined use of the polarimetric observables associated with the IPP and PRT spaces to characterize samples. Note that to the best of our knowledge, depolarizing spaces are nowadays used to discriminate among depolarizers,[16,17,35] but here, we use these observables for the first time to infer the physical inherent characteristics of samples inducing depolarization.

In particular, we first provide in Sec. 3.1.1 the method and conditions used to construct a full space of depolarizing simulations, which represent the targets to be studied in the IPP and PRT space frameworks. Then, in Sec. 3.1.2, we study the potential of these spaces to discriminate between diattenuator-based and retarder-based depolarizers. Finally, we analyze the potential of these two spaces to infer inherent structural information of one of these two depolarizers' origin, i.e., for the diattenuator-based depolarizer case (Sec. 3.1.3) and for the retarder-based depolarizers case (Sec. 3.1.4)

3.1.1 Method and conditions for depolarizing simulations

According to the parallel decomposition theory,[40] which states that any physically realizable depolarizer can be implemented as the incoherent addition of non-depolarizing polarimetric elements, we have simulated different depolarizers based on two different inherent origins: (1) diattenuator-based depolarizers, consisting of the incoherent addition of different linear diattenuators, and (2) retarder-based depolarizers, consisting of the incoherent addition of different retarders. Note that such resulting depolarizers belong to the polarization–anisotropy depolarizers class,[41] which in turn represent a significant number of samples existing in nature. Under this scenario, some control parameters are presented in the conducted model: the number N of elements in the summation; the orientation θ (corresponding to the transmission axis and fast neutral axis for the diattenuator-based and retarder-based cases, respectively) of each element; the diattenuation, D, for the diattenuator case; and the retardance, ϕ, for the retarder case, of each element.

For the diattenuator-based depolarizers simulations, we set the number of elements in the summation as $N = 300$ as a trade-off between a large number N, representing real scenarios, and an acceptable computation time. Afterward, the direction of each diattenuator within the summation could be set arbitrarily by generating random numbers. However, to mimic a scenario closer to real samples in nature (as could be the case of a distribution of collagen fibers in tissues or cellulose in the vascular tube of leaves), the directions of diattenuators were assigned to follow a Gaussian distribution, so each orientation is given by $\theta_m + \delta$, where θ_m is the orientation mean value selected from the range $(0, \pi)$, and δ follows a Gaussian distribution with a null mean and a given variance (σ^2). Lastly, the diattenuation value (D) of each diattenuator in the summation is changed from 0 to 1 with a customized step.

Similarly, for the retarder-based depolarizers simulations, the number of retarders N was also set to 300, and the directions assignation of such retarders was conducted in the same way as in the previous diattenuator-based depolarizer case. In turn, the retardance ϕ was employed to control the performance of each retarder, which ranges from 0 to π. More information

on the simulated MMs can be found in Ref. 41. Such parameters shown above for both retarder-based and diattenuator-based depolarizers, determining the depolarization of depolarizers, are named as microscopic parameters, in consideration of the fact that they cannot be measured by a macroscopic polarimeter.

3.1.2 Retarder-based and diattenuator-based depolarizer discrimination

As stated before, polarization–anisotropy depolarizers arise from the incoherent addition of two types of unitary structures: (a) dichroic materials (diattenuators) or (b) birefringent materials (retarders). Thus, our first goal is to evaluate if the considered IPP and PRT spaces are able to discriminate between these two depolarizer origins, without *a priori* information of the sample, and thus to infer information about the inherent structure of depolarizers. To do so, we follow the simulation conditions described in Sec. 3.1.1 to create a collection of diattenuator-based and retarder-based depolarizers.

On the one hand, for the diattenuator-based depolarizers, the mean orientation of diattenuators, θ_m, was set as to $\pi/3$. Note that we arbitrarily chose this mean orientation value as we realized in simulations that results are independent of this parameter, this being logical as it just represents a unitary rotation of the system, which does not modify the resultant polarimetric characteristics. At this stage, the controlling parameters for implementing different depolarizers remain the D coefficient and the orientation variance σ^2. To simulate a significant collection of different depolarizers, the D coefficient was set as a 1×10^4 value array by taking values from 0 to 1 (coefficient range) with a step of 10^{-4}. In the same way, the orientation variance σ^2 consisted of 10^4 different elements by taking values from 0 (all diattenuators pointing in the same direction) to $\pi/2$ (reasonable maxima orientation variance if considering real samples) with steps of $\pi/2 \times 10^{-4}$. This scenario led to $10^4 \times 10^4 = 10^8$ simulations of different diattenuator-based depolarizers.

On the other hand, a significant collection of retarder-based depolarizers was also constructed. The mean value for retarder orientation was fixed at $\pi/3$ by following the same criteria in the previous case. Analogously to the previous case, the retarder orientation variance σ_2 was also set as an array of 10^4 elements with values from 0 to $\pi/2$ with steps of $\pi/2 \times 10^{-4}$. Finally, the retardance ϕ consisted of 10^4 elements by taking values from 0 to π with a step of $\pi \times 10^{-4}$. Consequently, we also implemented 10^8 simulations for retarder-based depolarizers.

Then, the IPP- and PRT-associated observable values (as described in Sec. 2, P_1, P_2, and P_3 for IPP and P, R, and T for PRT spaces) were calculated for these 2×10^8 simulated depolarizers (10^8 diattenuator-based depolarizers and 10^8 retarder-based depolarizers), and the corresponding spatial points are represented in the IPP and PRT spaces in Figs. 3(a) and 3(b), respectively. To provide another perspective to analyze the distribution of such points, the plane of $P_3 = 1$ in IPP space and the plane of $T = 0$ in PRT space are illustrated in Figs. 3(c) and 3(d), respectively. Note that the points representing diattenuator-based and retarder-based depolarizers are colored in red and green, respectively.

By analyzing the data represented in both spaces, we realize that they present a certain potential to discriminate between the origin of the simulated depolarizers (diattenuator-based or retarder-based depolarizers). However, we see how the PRT space is much more suitable for discriminating between these two depolarizer origins than the IPP space. In particular, although all simulated depolarizers are placed at the top surface of the IPP space [P_1P_2 space for $P_3 = 1$; see Fig. 3(a)],

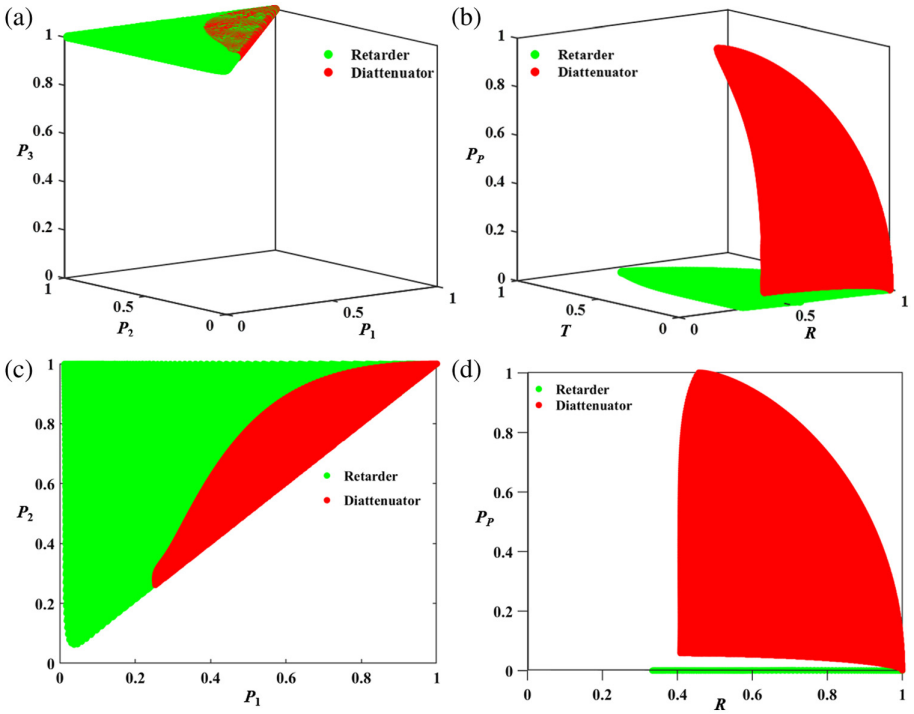

Fig. 3 Distributions of diattenuator-based (red color) depolarizers and retarder-based (green color) depolarizers represented in the studied depolarizing spaces. (a) IPP space. (b) PRT space. (c) Plane of $P_3 = 1$. (d) $T = 0$ in the PRT space.

independently of the physical origin (red and green data), the discrimination is much more efficient using the PRT space because depolarizers are distributed all over the volume [Fig. 3(b)]. This plane restriction associated with the IPP space is well understood if considering that we are dealing with polarization–anisotropy depolarizers, and thus, no contribution of polarization–isotropy depolarization is present in the simulated systems (i.e., only the $P_3 = 1$ is available, and this condition makes the polarization–isotropy contribution equal to zero[41]). This spatial limitation when representing polarization–anisotropy depolarizers within the IPP space leads to an overlap of data [see green–red overlapped region at the top surface of IPP space in Fig. 3(c)] corresponding to depolarizers of different origins (i.e., the overlap of red and green data in some cases). In other words, the IPP space presents some ambiguities for certain depolarizers. This scenario states that some different physical systems, both diattenuator-based and retarder-based depolarizers, may lead to the same depolarizer representation in the IPP space, and this situation constitutes the lack of discrimination potential when dealing with the IPP space.

In contrast to that, the PRT space arises as a suitable tool for discriminating between diattenuator-based and retarder-based depolarizers, providing complete description without ambiguity. In particular, although retarder-based depolarizers are located at the $P_P = 0$ plane [see green data in Fig. 3(b)], the diattenuator-based depolarizers [red data in Fig. 3(b)] are located at the rest of the PRT volume (they are distributed out of the plane $P_P = 0$). This situation, providing a complete discrimination between diattenuator-based and retarder-based depolarizers, arises from the nature of the PRT space. In particular, as P_P observable deals with the dichroic behavior of samples, it should be always zero when dealing with retardance origin, and thus, retarder-based depolarizers are in this plane. Analogously, diattenuator-based depolarizers should present certain non-zero values for P_P, so they must be out of the $P_P = 0$ plane. As a consequence, the PRT space provides an ideal framework for such diattenuation-retarder depolarizer discrimination. Note that there exists only one point in the PRT space where the two physical origins overlap [point $P_P = 0$, $R = 1$, and $T = 0$; see Fig. 3(d)], and this is just the case where MM of the related sample is diag(1, 1, 1, 1) (i.e., the identity matrix). This point corresponds to systems with the ϕ and D values equal to 0 for retarder-based and diattenuator-based depolarizers respectively, but under this condition, they degenerate to be a polarization–isotropy media without any polarization effect (non-polarimetric system).

At this point, it is worth recalling that we selected the IPP space from different depolarizing spaces proposed in the literature because it proved to be an excellent candidate for depolarizer discrimination.[35] Thus, the results and discussion shown in this subsection provide that the PRT space is an excellent approach for depolarizing sample description, overcoming the discriminatory performance of other existing alternatives in terms of origin (dichroic-birefringent) characterization.

Note that the present work has focused on linear anisotropies (diattenuator-based or retarder-based depolarizers) because they represent important real scenarios; for instance, it is the case of vegetal or animal tissues. In fact, animal tissues, rich in collagen fibers, may give rise to retarder-based depolarizers, and vegetal tissues, rich in cellulose, may give rise to diattenuation-based depolarizers.[20] However, other more complex depolarizing scenarios may arise from mixtures of retarder and diattenuator unitary elements. For readers interested in such cases, a discussion about retarder-based and diattenuator-based depolarizers is included in Sec. 4 in the Supplementary Material, where we demonstrated that the proposed methods are also valid to discriminate these situations, being especially relevant for such purposes of PRT space.

As a final remark, we want to emphasize that when focusing on a particular type of depolarizing origin (red or green data), we see that different control parameters lead to different locations of the resulting depolarizes at both the IPP and the PRT spaces. In particular, different locations for diattenuator-based depolarizers (red data) are associated with different orientations or deviations of diattenuation or different diattenuation values, and in the same vein, different locations for retarder-based depolarizers (green data) are associated with different orientations or deviations of the fast axis of the retarders or different retardance values. Thus, the simulations in Fig. 3 indicate that such spaces have the potential to discriminate among different internal structures leading, on the one hand, to diattenuator-based depolarizers and, on the other hand, to retarder-based depolarizers. The aim of the following subsections is to delve into this topic with the aim of inferring more inherent information about depolarizers and thus characterize diattenuator-based depolarizers (Sec. 3.1.3) and retarder-based depolarizers (Sec. 3.1.4).

3.1.3 Characterization of diattenuator-based depolarizers with different structural characteristics

In this section, we study the suitability of the IPP- and PRT-associated polarimetric observables to characterize depolarizers with a common origin, that is, diattenuator-based depolarizers, but with different inherent structural characteristics. To this aim, we implement a collection of diattenuator-based depolarizer simulations with different controlling parameter values. As in the previous section, and by following the simulation conditions described in Sec. 3.1.1, each generated depolarizer is composed of the incoherent addition of $N = 300$ linear diattenuators. The D is set as an array of 10^4 elements uniformly distributed between [0, 1]. In addition, the occupied space of simulations is increased by repeating the above simulation patterns for different values of the standard deviation σ^2 associated with the Gaussian distribution of the diattenuator orientation. In particular, we use values of σ^2 from 0 to 0.5π, with a step of 0.05π, so 11 different cases are formed. Under this scenario, $10^4 \times 11 = 1.1 \times 10^5$ different diattenuator-based depolarizers are simulated, represented in the PRT and IPP spaces in Figs. 4(a) and 4(b), respectively.

Figure 4 illustrates the spatial distributions of simulated diattenuator-based depolarizers at such spaces as a function of different D and σ^2 values, in which varying colored curves correspond to diattenuator-based depolarizers with different values of the parameter σ^2 (provided in Fig. 4 legend). In other words, each curve represents the depolarizers with the identical σ^2, at which different points represent the depolarizer with varying D.

The corresponding distribution results demonstrate the certain ability of PRT and IPP spaces to distinguish among the depolarizers with the same origin but different inherent structural characteristics. In particular, the represented depolarizers occupy a vast volume in such spaces. In theory, the IPP and PRT spaces are able to represent all depolarization systems, and furthermore, each position in such spaces represents the case with unique polarization characteristics. In addition to

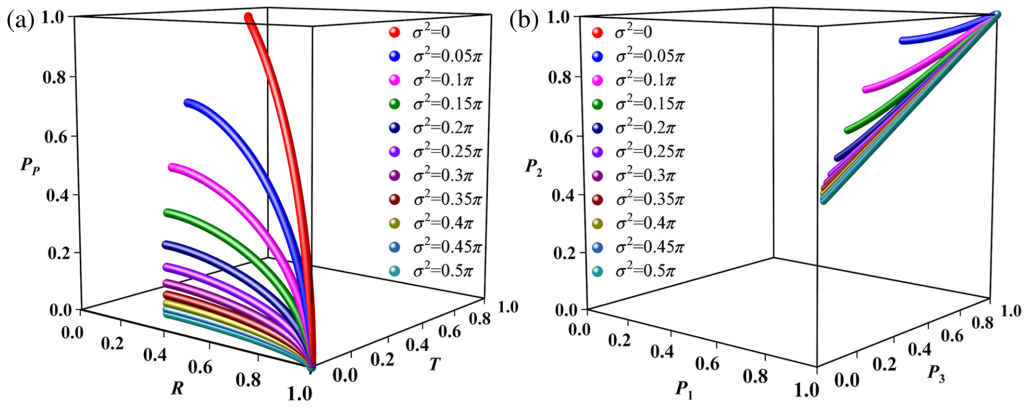

Fig. 4 Representation of the simulated diattenuator-based depolarizers in different representation spaces. (a) PRT space. (b) IPP space.

demonstrating the fact that depolarizers with different structural characteristics represent unique physical properties, the vast volume that the depolarizers occupy also implies the possibility of being distinguished. In particular, in the IPP space, shown in Fig. 4(b), the distances between the curves corresponding to σ^2 values smaller than 0.15π are significant, ensuring clear discrimination among systems, but as σ^2 increases, the corresponding curves become closer, this situation becoming more critical for curves related to values of σ^2 bigger than 0.25π, where the curves have become nearly indistinguishable. Conversely, the PRT space shows a better performance in distinguishing among lines representing depolarizers with different σ^2. In particular, the related lines have clearly different behaviors, especially when σ^2 is smaller than 0.35π (it is a common range in biological tissues), which demonstrates the ability of PRT space to identify different diattenuator-based depolarizers.

Comparing curves with different controlling parameters, we realize that with the increase of σ^2, the corresponding curves get close to the plane ($P_P = 0$) in PRT space. Recall that in the current study, the inherent elements being incoherently added to create a diattenuator-based depolarizer, are pure diattenuators with different orientations. As σ^2 becomes larger, the orientation dispersion of the inherent elements increases, decreasing the overall diattenuation D for the resultant depolarizer (note that as a larger number of orientations are considered more orthogonal, systems cancel their diattenuation properties among them). Therefore, the polarimetric observable P_P arises as a nice indicator of the dispersive distribution of internal units in a depolarizer. By taking profit of this correlation between P_P and σ^2, we could explore the idea of implementing an analytical relation describing the orientation dispersion characterized by σ^2 as a function of the observable P_P. This situation is further studied in Sec. 3.3. In addition, more details about the connection between P_P observable and σ^2 can be consulted in the Supplementary Material.

In summary, both such polarization spaces are certainly capable of characterizing the diattenuator-based depolarizers with different structural characteristics, and moreover, PRT space shows significant superiorities over IPP space in several tasks. On one hand, whereas all diattenuator-based depolarizers fall on a fixed plane ($P_3 = 1$) in IPP space, PRT space illustrates a 3D distribution with a big volume of all diattenuator-based depolarizers, which leads to representing points of such depolarizers have bigger geometrical distance and less overlap in PRT space. On the other hand, as stated in Sec. 2.2, unlike IPP space only containing the amplitude of randomness, the observables in PRT space have physical meaning, leading to PRT space performing better in analyzing diattenuator-based depolarizers. In particular, whereas IPP space cannot distinguish among pure systems with different structures, PRT space can identify the structure of pure systems.

3.1.4 *Characterization of retarder-based depolarizers with different structural characteristics*

As a complement of Sec. 3.1.3, in this section, we study the suitability of the IPP- and PRT-associated polarimetric observables to characterize depolarizers originated by the incoherent addition of linear retarders, that is, retarder-based depolarizers. To this aim, we implement a collection of retarder-based depolarizer simulations with different controlling parameter values. For consistency with the previous sections, the generated depolarizers are composed of the incoherent addition of $N = 300$ linear retarders, and the mean orientation is once again set to $\pi/3$ (recall that this last value is arbitrarily chosen because it is not significant in terms of polarimetric performance of resulting depolarizers). In this case, the multiple retarder-based depolarizers are generated by properly setting the retardance (ϕ) value for constituent retarders and the deviation value σ^2 from the mean orientation, which, as previously discussed, obeys the Gaussian distribution. It means the physical properties of the formed retarder-based depolarizers depend on the parameters σ^2 and ϕ. In particular, the retardance ϕ was set as an array of 11 elements by taking values from 0 to π with a step of 0.1π. In addition, the neutral line orientation deviation σ^2 of the constituent retarders was set as an array of 10^4 elements by taking values from 0 to π with a step of $\pi\times10^{-4}$. Note that the possible combinations led to 1.1×10^5 simulated retarder-based depolarizers, which were represented, as shown in Fig. 5, at the RT [Fig. 5(a)] and P_1P_2 [Fig. 5(b)] planes belonging to the PRT and IPP spaces, respectively.

Note that we restrict the representation to corresponding planes instead of the complete volume spaces because, as described in Sec. 2, retarder-based depolarizers can only be contained in such planes. Unlike diattenuator-based depolarizers discussed above, the results in this section for retarder-based depolarizers are arranged as different curves with varying ϕ. Under this condition, the points at each cure represent the depolarizers with the same ϕ but different σ^2.

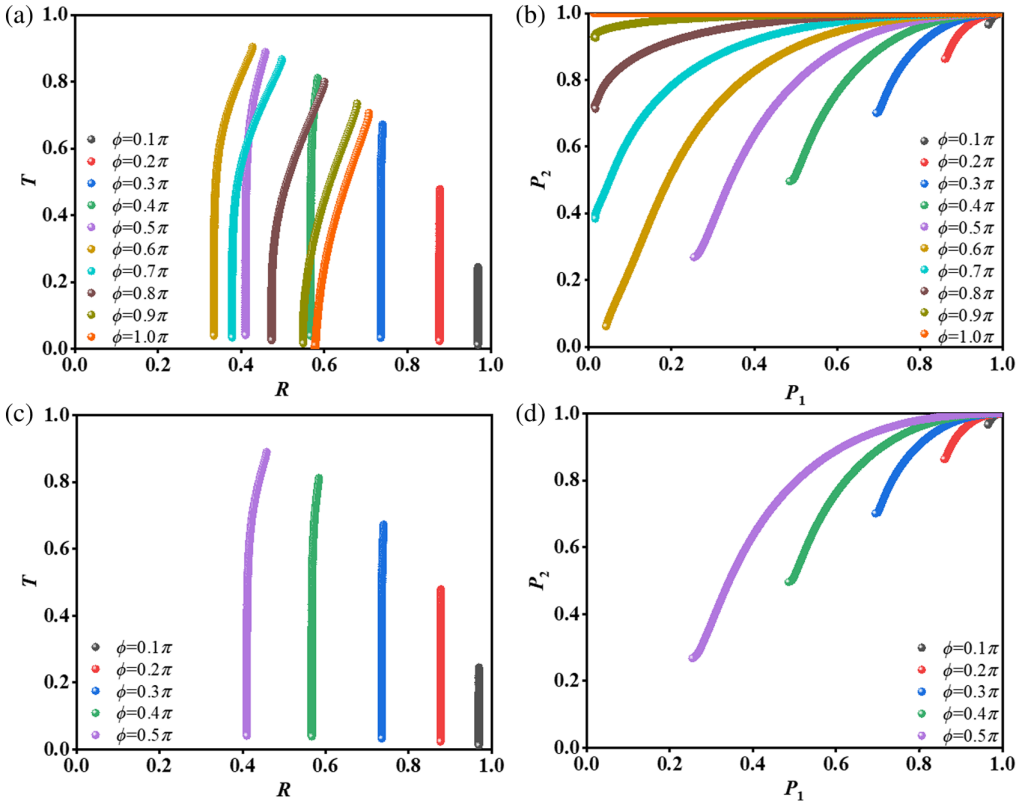

Fig. 5 Retarder-based depolarizers corresponding to different control parameters represented at the P_1P_2 and RT spaces. (a) RT space with full range. (b) P_1P_2 space with full range. Depolarizers spatial variation with σ^2 in the (c) RT space with retardance ϕ smaller than 0.5π and the (d) P_1P_2 space with retardance ϕ smaller than 0.5π.

It is worth noting that a case of $\phi = 0$ representing the units within retarder-based depolarizer entirely lose the retardance. Analogous to the case of $D = 0$ resulting in a diattenuator-based depolarizer in a pure system, this case leads the retarder-based depolarizer to degenerate to a polarization–isotropy media, which is represented by a single point ($P_1 = 1$, $P_2 = 1$ in P_1P_2 space, $R = 1$, $T = 0$ in RT space). According to the 10 values of retardance ϕ selected [see legend in Figs. 5(a) and 5(b)], we represent 10 different curves where each point of a particular curve represents a different value of σ^2. We see how the observable R presents an important discriminatory capability to classify different retarder-based depolarizers with different retardance ϕ values within a range of ϕ = (0.1π and 0.5π), as seen in Fig. 5(c). In addition, we also see that the observable T presents discriminatory capability with σ^2, being more sensible to this parameter as larger the retardance value [larger curves in Fig. 5(c)]. Therefore, the combination of observables T and R arises as a nice framework to study the inherent characteristics of retarder-based depolarizers, as is the case of the retardance ϕ and the dispersion σ^2. However, when we deal with retardance-based depolarizers with larger retardance ϕ values [see larger ϕ range in Fig. 5(a), $\phi = (0.1\pi, \pi)$], the newly analyzed curves overlap with those previously studied in Fig. 5(c), which leads to an ambiguity in the determination of the retardance parameter.

If the same study is conducted in terms of the P_1P_2 space [see Figs. 5(b) and 5(d)], the same discriminatory potential is observed for the ϕ = (0.1π and 0.5π) range, as a combination of P_1P_2 observables [see Fig. 5(d)], but unlike for the RT plane case, the P_1P_2 space still presents certain discriminatory potential for the full range $\phi = (0.1\pi, \pi)$, although the sensibility decreases as the ϕ value increase [see Fig. 5(b)]. Therefore, simulated results in Fig. 5 provide that IPP space performs better than PRT space because the IPP space effectively avoids the ambiguity in ϕ discrimination. However, there is still a problem with P_1P_2 space for large values of ϕ, in which, for instance, curves only share a limited area and thus the distance between curves is notably reduced (loss of sensitivity for larger ϕ values). A more detailed description of the selected observables and model parameters is provided in the Supplementary Material.

Last but not least, we want to note that data in Fig. 5 provide a certain correlation among polarimetric observables, as R and T, and physical parameters, as ϕ and σ^2, thus paving the way to implement physical models based on R and T macroscopic measurements for microscopic parameters determination. This idea is further explored in Sec. 3.3.

There are other scenarios that can also be represented in nature, as is the case of systems with the same unitary element orientations but presenting a dispersion in the mean polarimetric value, that is, dispersion on the retardance for retardance-based depolarizers and dispersion in the diattenuation in the diattenuation-based depolarizers. This situation is explored and discussed in Sec. 3 in the Supplementary Material, but the main conclusion is that the combination of the IPP and PRT spaces is also suitable for distinguishing depolarizers originated by different dispersion values of the mean polarimetric parameter.

3.2 Experimental Results

In this section, we provide the experimental validation of the methods provided in Sec. 3.1. This is achieved by conducting diverse phantom experiments trying to reproduce some of the depolarizers simulated in Sec. 3, with the aim of validating the provided conclusions. To do so, we measured the experimental MM of a polarizer and of a quarter-wave plate (Meadowlark Optics, Frederick, Colorado, United States) at different orientations, using a complete imaging polarimeter. The experimental MMs were obtained by the complete imaging polarimeter sketched in Fig. 6.

The light source of the polarimeter is a multiwavelength light emitting diode (LED) source where red light (the wavelength centered at 625 nm with a narrow band of 10 nm) is employed. Then, the input light (illuminating samples) is modulated by the polarization state generator (PSG), composed of a linear polarizer and two liquid crystal retarders (LCR1 and LCR2). Incident light beam with customized polarization then illuminates studied samples (herein the polarizer and quarter wave plate). Light exiting from samples after polarimetric transformation is analyzed by a subsequent polarization state analyzer (PSA), composed of other two LCRs, and a linear polarizer. Finally, images of the studied sample plane are obtained with a standard CCD camera with an exposure time of 100 ms (Allied Vision Manta G-504B). By taking into account the linear relation between input and output polarizations through MMs, by properly selecting an array of input polarizations, and detecting the related polarizations exiting from the sample, the complete MM of analyzed samples can be readily obtained. Notably, before measuring the studying sample, the MM polarimeter is calibrated, and the condition number is 1.85. More details about polarimeter calibration and MMs measurement referent to the used polarimeter can be obtained in Ref. 54.

Using the above-described polarimeter, the experimental MMs of the polarizer and the quarter-wave plate samples were measured in both cases for 1800 equidistant orientations (from 0 to π with steps of $\pi/1800$). Note that from this MM database, by properly incoherently adding experimental MMs, we can implement diverse experimental depolarizers. According to the manufacturer's technical specification, the transmission coefficients for the polarizer used in experiments are larger than 0.82 and the extinction ratio is larger than 683:1. In the case of the waveplate used, the retardance is $\pi/2$ for 625 nm, so it behaves as a quarter-waveplate for this wavelength. Under this scenario, we can implement different depolarizers by controlling the orientation standard deviation σ^2 (set to follow a Gaussian distribution) when incoherently adding the measured MMs. Therefore, we implemented a collection of different experimental diattenuation-based depolarizers and retarder-based depolarizers as a function of different σ^2 values. The obtained results are represented at the PRT and P_1P_2 spaces (see Fig. 7). In addition, the associated simulated results, considering an ideal polarizer ($D = 1$) and an ideal quarter-waveplate ($\phi = \pi/2$), are also provided in Fig. 7 for comparison. In the case of the experimental quarter-waveplate, we found that the experimental MM presented slight diattenuation values (0.036) that can be related to Fresnel coefficients in reflection and refraction processes at the waveplate entrance-exiting faces. Furthermore, we applied a Lu–Chipman decomposition method,[45] which decomposes any MM as the product of a depolarizer matrix, a pure retarder matrix, and a pure diattenuator matrix to the experimentally obtained Mueller matrices. Then, the data presented in Fig. 7 for the retarder case are just that obtained from the Lu–Chipman derived Retarder matrix, as this situation removes possible diattenuation and depolarizing contributions, which ensures a closer comparison with the theoretical pure retarder. As stated in the Fig. 7 legend, simulated results are provided in red, whereas experimental results are provided in blue. We obtain an excellent agreement between simulated and experimental results, providing the validity of the proposed methods. Note that for the P_3 axis, the range is restricted between 0.75 and 1.1 for better visualization of data.

In particular, the represented data curves clearly demonstrate that simulations and experiments present an excellent match as a function of different orientation variances σ^2 (different points in each curve). To quantificationally represent the discrepancy among them, the mean square error (MSE) of the distance between points representing the simulation and experiment with the same setups are calculated. The MSEs of Figs. 7(a)–7(d) are 0.027, 0.030, 0.026, and 0.029, respectively. Note that these small differences among simulated-experimental data are mainly associated with non-ideal experimental elements (polarizer and quarter-waveplate) used in the experiments. In particular, the polarizer sample shown, for the wavelength used in the experiments (625 nm), the diattenuation is 0.97, whereas according to the Lu–Chipman decomposition approach, the quarter-waveplate presented an experimental retardance of $f = 0.53\pi$. Besides, as shown in Fig. 7, the experimental results illustrate that the polarizer-based depolarizers and quarter-wave plate–based depolarizers lie on different surfaces. This confirms the discussion provided in the previous simulation (Sec. 3), that is, a new criterion to distinguish between diattenuator-based and retarder-based depolarizers is here presented.

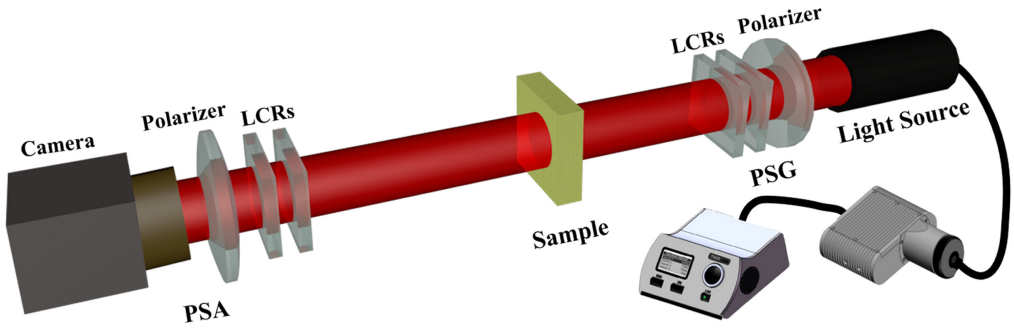

Fig. 6 Scheme of the MM polarimeter.

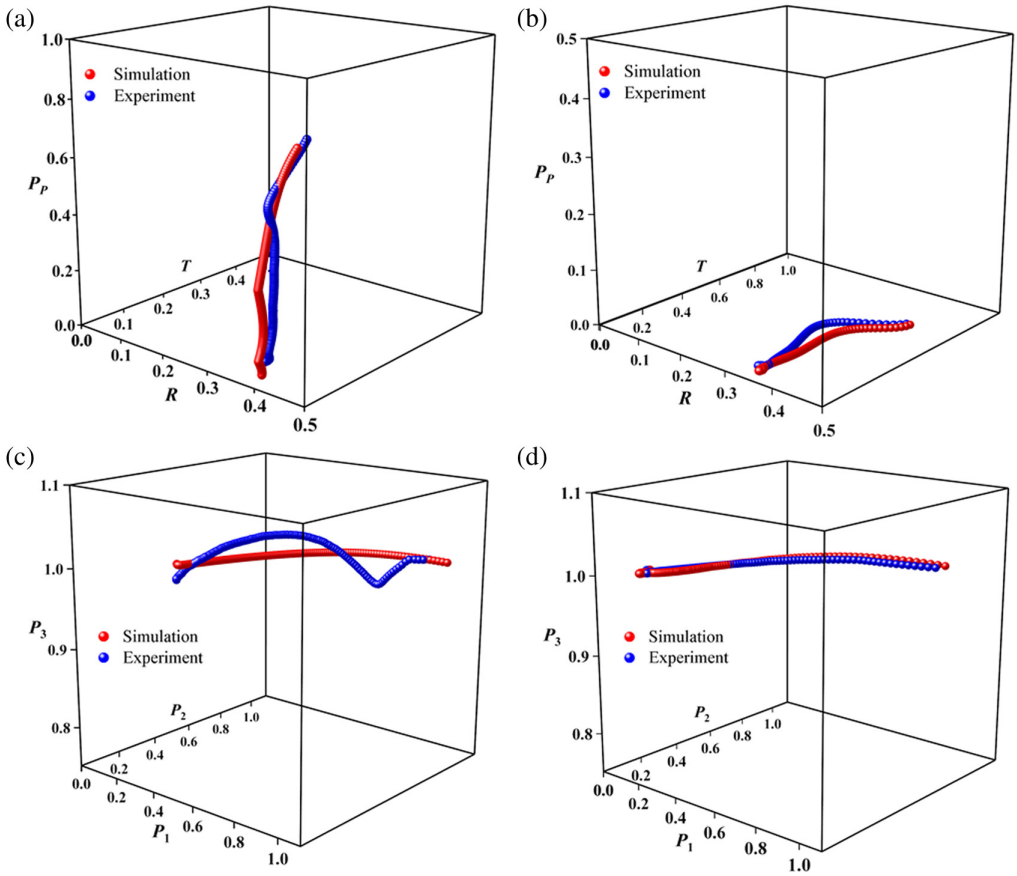

Fig. 7 Comparison between simulations and experiments in the studied space for different samples with varying σ^2. (a) Distributions with σ^2 for diattenuator-based depolarizers in PRT space. (b) Distributions with σ^2 for retarder-based depolarizers in PRT space. (c) Distributions with σ^2 for diattenuator-based depolarizers in IPP space. (d) Distributions with σ^2 for retarder-based depolarizers in IPP space.

3.3 Physical Parameter Sample Characterization from PRT Space Polarimetric Observables

As analyzed in Sec. 3.1, depolarizers consist of a large number of units whose polarization properties determine the macroscopic polarization features of the resulting depolarizers. Furthermore, Sec. 3.1 has paved the way to correlations among inherent physical characteristics of depolarizers with polarimetric observables. In this vein, the goal of this section is to implement a physical model, based on polarimetric observable data, able to retrieve inherent information of samples. In particular, we develop diverse models, based on the PRT space observables, characterizing the physical features of diattenuator-based depolarizers (Sec. 3.3.1) and retarder-based depolarizers (Sec. 3.3.2). We selected the PRT observables to implement the models because, according to Sec. 3.1 discussion, they have proved a superior performance in terms of sample characterization. Note that this is the first attempt presented in the literature to characterize microscopic information of samples from macroscopic depolarizing measurements.

3.3.1 Calculating physical characteristics of diattenuator-based depolarizers

We recall that the diattenuator-based depolarizers were obtained from the incoherent addition of a series of diattenuator with a given diattenuation D and orientation dispersion indicated by the covariance σ^2. As stated in Sec. 3.1, there is a clear correlation between P_p observable and σ^2. In addition, further analysis of connections between PRT observables and physical features has shown us that there is also a strong correlation between the observable R and the diattenuation D of the correspondent depolarizers. Importantly, R observable is independent of σ^2, so we find a direct link between polarimetric measurement R with physical feature D associated with diattenuator-based depolarizers. This independency of σ^2 with diattenuation is provided in Fig. 8(a), where the results clearly illustrate that all curves with different σ^2 marked in different colors are totally coincident (overlapped) along the same trajectory. Afterward, by taking profit of the direct relation between D and R, we implemented an analytical function of D dependent on R parameter, allowing us to predict D values from R measurements. To do so, we implemented a polynomial fit on data in Fig. 8(a), leading to the following analytical equation:

$$D(R) = -196.6R^5 + 671.39R^4 - 903.08R^3 + 595.4R^2 - 192.43R + 25.39. \quad (13)$$

To verify the accuracy of Eq. (13) in terms of predicting D from R measurements, the experimental database measured in

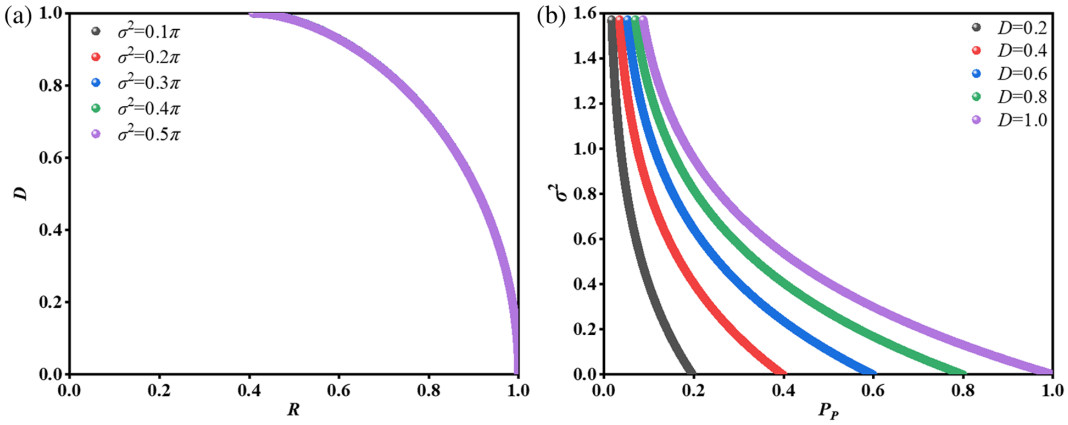

Fig. 8 Relation between the measured polarimetric and physical characteristics for diattenuator-based depolarizers. (a) Relation between D and R at different σ^2. (b) Relation between P_P and σ^2 at different D.

Sec. 3.2 (1800 equidistant orientations of polarizer from 0 to π with steps of $\pi/1800$) is employed to construct the diattenuator-based depolarizers with different σ^2. In particular, based on the measurement of the polarizer at different orientations, we constructed 300 depolarizers whose σ^2 was modified from 0 to 0.5π with the step of $\pi/600$. At this stage, we calculated the corresponding R value for each implemented depolarizer. Afterward, the polarimetric observable D is calculated using Eq. (13) with R as the only independent variable. Note that all depolarizers were constructed from the same experimental polarizer, so they share the same D value, and according to the previous analysis, the same R value. Under this scenario, independently of the different σ^2 evaluated all depolarizers must provide the same diattenuation response. The obtained results show an excellent agreement between the average of experimental D_{exp} values ($D_{\text{exp}} = 1.04 \pm 0.03$) and the expected value $D = 0.97$. Note that the slight differences are accounted for by errors associated with the experimental measurement, which are related to instrumental sources such as illumination bandwidth or polarizer misalignments from measurement to measurement.

The next step is to build a second model able to predict σ^2 from polarimetric observables. As previously discussed, the observable P_P is especially suitable for this aim. For the sake of clarity, Fig. 8(b) states this link between σ^2 and P_P for diattenuator-based depolarizers related to different D values [see the legend in Fig. 8(b)] which are perfectly discriminated by the P_P observable [X-axis in Fig. 8(b)]. Note that different curves (colors) relate to different D values, which are perfectly determined from R observable, as provided by Eq. (13).

To implement the analytical function relating σ^2 with P_P measurements, we chose an arbitrary curve $D = 1$ [see the violet curve in Fig. 8(b)]. Note that this approach is reasonable as in experimental implementations, we can determine the proper D by Eq. (13) and then, fix it to be applied in the following approach. At this point, the $D = 1$ curve was fitted to a polyonomy and the obtained results are presented in the following equation:

$$\sigma^2(P_P, D=1) = -20.92P_P^5 + 63.14P_P^4 - 73.61P_P^3 + 42.25P_P^2 - 13.31P_P + 2.42. \quad (14)$$

To test the validity of Eq. (14), we implemented experimental depolarizers by arbitrarily assigning different σ^2 to the incoherent additions (see the third column in Table 1). From the corresponding obtained Mueller matrices of implemented depolarizers, the experimental P_P values were calculated (see first column in Table 1). Finally, these P_P values were applied to Eq. (14), obtaining the corresponding calculated σ^2 (see second column in Table 1). We obtain an excellent agreement between experiments and calculations as can be observed from absolute errors between assigned and calculated values (see fourth column in Table 1) as well as from the mean absolute error ($\sim$1% error).

3.3.2 *Calculating physical characteristics of retarder-based depolarizers*

As a continuation, we aim to calculate the physical characteristics of retarder-based depolarizers. Recall that the physical characteristics of retarder-based depolarizers consisted of retarders with different retardance ϕ and orientation distribution σ^2. As stated in Sec. 3.1, there is a clear correlation between R observable and ϕ, where the represented curves with different ϕ are almost perpendicular to the X axis [when ϕ is smaller than 0.5π, see Fig. 5(c)]. Importantly, further analysis demonstrates that the observable R is independent of σ^2, and what is more, only dependent on ϕ. To prove this statement, the relation between R and φ with different σ^2 is illustrated in Fig. 9(a), in which all curves are marked in different colors representing varying σ^2. Note that all curves are totally coincident

Table 1 Difference (rad) between calculated σ^2 and assigning σ^2 for diattenuator-based depolarizers.

P_P	Calculated σ^2	Assigning σ^2	Absolute error
0.3	0.7026	0.7355	0.0329
0.4	0.5471	0.5516	0.0045
0.5	0.4188	0.4203	– 0.0015
0.6	0.3004	0.3100	– 0.0096
0.7	0.2012	0.2101	– 0.0089
0.8	0.1308	0.1156	0.0152
0.9	0.0749	0.0578	0.0171
Mean absolute error			0.0128

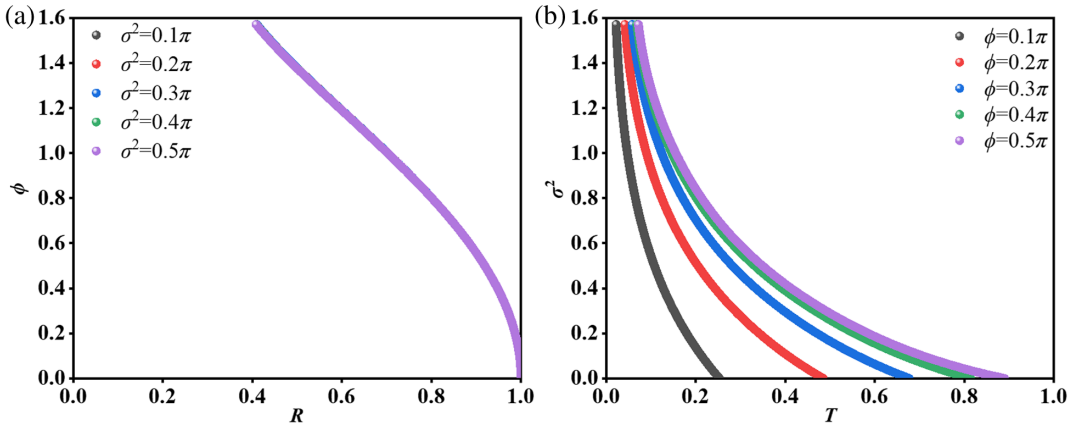

Fig. 9 Relation between the measured polarimetric and physical characteristics for retarder-based depolarizers. (a) Relation between ϕ and R at different σ^2. (b) Relation between σ^2 and T at different ϕ.

independently on σ^2, indicating that ϕ can be calculated by the polarimetric observable R as a single variable. Under this situation, we fitted with a polynomial relation data in Fig. 9(a), leading to the following analytical equation:

$$\phi(R) = -9.54R^3 + 18.41R^2 - 13.42R + 4.56. \tag{15}$$

To confirm the illustrated relation between ϕ and R [see Eq. (15)], the data of the quarter-wave plate measured in Sec. 3.2 (1800 equidistant orientations of the quarter-wave plate from 0 to π with steps of $\pi/1800$) were employed to construct the retarder-based depolarizers with different σ^2. In particular, the 300 retarder-based depolarizers with different σ^2 were constructed, and the R of each consisting depolarizer is calculated to obtain ϕ. In this scenario, all depolarizers were constructed from the same experimental waveplate sharing the same ϕ value, so all generalized retarder-based depolarizers with different σ^2 should provide almost the same retardance response. Accordingly, the obtained average of the calculated retardances was $\phi_{\text{exp}} = 1.72 \pm 0.03$. Compared with the expected value ($\phi = 1.66$ of the measured quarter wave), the small difference proves the applicability of Eq. (15).

Afterward, we developed a model able to predict σ^2 from polarimetric observables. As previously discussed, whereas the polarimetric observable P_P of retarder-based depolarizers always equals 0, due to the absence of diattenuation in retarder-based depolarizers, only observable T is left and it is sensitive to the change of σ^2 [see Fig. 5(a)]. For this reason, the relation between σ^2 with T at different ϕ values is represented in Fig. 9(b), in which the different ϕ relates to different color curves. Observed dependences indicate that σ^2 is able to be calculated from observable T after we calculate the value of ϕ by R through Eq. (15). To implement the way of calculating σ^2 with observable T measurements, we chose an arbitrary curve $\phi = 0.5\pi$ [see the violet curve in Fig. 9(b)] and fitted it to a polyonomy presented in the following equation:

$$\sigma^2(T, \phi = \pi/2) = -38.12T^5 + 101.19T^4 - 103.44T^3 + 52.19T^2 - 14.60T + 2.34. \tag{16}$$

Finally, to test the validity of Eq. (16), we experimentally obtain the T value from experimental Mueller matrices of implemented retarder-based depolarizers constructed from the controlled incoherent addition of experimental waveplate (see the first column in Table 2), by arbitrarily assigning different σ^2 (see the third column in Table 2). Afterward, these T values were applied to Eq. (16) to obtain the corresponding calculated σ^2 (see the second column in Table 2). The experiments and calculations represent an excellent agreement, as can be observed from absolute errors between assigned and calculated values (see the fourth column in Table 2) as well as from the mean absolute error ($< 2\%$ error).

In summary, the PRT polarimetric observables are excellent tools to retrieve microscopic physical characteristics from macroscopic polarimetric measurements. In particular, the polarimetric observable R is suitable to calculate the diattenuation D and retardance ϕ for diattenuator-based and retarder-based depolarizers, respectively. With this prior information of the exact values of diattenuation D and retardance ϕ, the orientation distribution σ^2 of elementary units generating depolarization within the samples, can be calculated by, on the one hand, the relation between σ^2 and P_P, provided in Fig. 8(b), and on the other hand, the relation between σ^2 and T, provided in Fig. 9(b).

Table 2 Difference (rad) between calculated σ^2 and assigning σ^2 for retarder-based depolarizers.

T	Calculated σ^2	Assigning σ^2	Absolute error
0.3	0.5912	0.5734	0.0178
0.4	0.4304	0.4255	0.0049
0.5	0.2906	0.3047	–0.0141
0.6	0.1754	0.1839	–0.0085
0.7	0.1021	0.1103	–0.0082
0.8	0.0566	0.0525	0.0041
0.9	– 0.0526	0.0105	–0.0631
Mean absolute error			0.0172

4 Conclusion

In this paper, we combined PRT and IPP spaces to infer the physical properties of different depolarizers, i.e., diattenuator-based depolarizers and retarder-based depolarizers constructed according to parallel decomposition. Although IPP space describes the magnitude of randomness induced by the interacted samples with incident polarized light, PRT space emphasizes the physical properties related to depolarization. For this reason, the information expressed by such two polarization spaces is complementary, which provides the possibility of identifying and analyzing the studying depolarizers. In particular, PRT space is capable of distinguishing retarder-based depolarizers from diattenuator-based depolarizers, as well as maximizing the discrepancy (geometrical distance) of different depolarizers with the same origin but different controlling parameters. However, ambiguity points, in PRT space, for retarder-based depolarizers, appear once the controlling parameters are beyond a threshold (herein ϕ about equals 0.6π). As expected, the threshold can be recognized in IPP space, and moreover, the space is able to further distinguish among the depolarizers represented by the ambiguity points in PRT space. Importantly, the proposed method also has the capacity to discriminate more complex polarization-anisotropic scenarios, that is, the depolarizers contain both depolarizers and diattenuators inside. Most importantly, although the depolarizers studied in this paper are polarization–anisotropy, the proposed method is able to analyze the samples containing polarization–isotropy depolarization, though being implemented on the polarization–anisotropy part in the samples. The only restriction of the method is to discriminate among different ideal depolarizers as in such systems, all polarization information of how depolarization was generated is lost.

Next, the results are verified by the measurement of a polarizer and a quarter-wave plate with different directions to construct depolarizers with different σ^2. The illustrated data in both IPP and PRT spaces demonstrate the consistency between the simulation and measurement, proving the correction of the results from the simulation illustrated in this paper. Finally, we provide a method to characterize the microscopic physical features of depolarizers from macroscopic polarization measurements associated with PRT space observables. As a proof of concept, we implemented diverse models that have proved to be suitable for the accurate determination of significant parameters of diattenuator-based depolarizes, as the diattenuation D of microscopic elements, of retarder-based depolarizers, as the retardance φ of microscopic elements, and the corresponding orientation distribution described by σ^2 in both cases. In this regard, the relevance of some observables as R, T, and P_P was highlighted.

In summary, we demonstrated that the combined use of the PRT and IPP spaces conforms to a suitable framework to accurately infer relevant microscopical properties of samples that are coded in their macroscopic depolarizing response. Methods provided in this work are general and of potential interest in all those applications dealing with depolarizing samples. In this sense, they could play a vital role in a vast number of applications such as material characterization, biological tissue identification, and pathology early detection both in botanical and biomedical fields.

Disclosures

The authors declare no conflicts of interest.

Code and Data Availability

Data underlying the results presented in this paper are not publicly available at this time but may be obtained from the authors upon reasonable request.

Acknowledgments

This work was supported by the China Scholarship Council (Grant No. 202306690024), the Ministerio de Ciencia e Innovación and Fondos FEDER (Grant Nos. PID2021-562 126509OB-C21 and PDC2022-133332-C21), the Generalitat de Catalunya (Grant No. 2021SGR00138), and the Beatriu de Pinós Fellowship (Grant No. 2021-BP-00206).

References

1. J. Tyo et al., "Review of passive imaging polarimetry for remote sensing applications," *Appl. Opt.* **45**, 5453–5469 (2006).
2. C. He et al., "Polarisation optics for biomedical and clinical applications: a review," *Light Sci. Appl.* **10**, 194 (2021).
3. C. He et al., "Characterizing microstructures of cancerous tissues using multispectral transformed Mueller matrix polarization parameters," *Biomed. Opt. Express* **6**, 2934–2945 (2015).
4. M. Dubreuil et al., "Linear diattenuation imaging of biological tissues with near infrared Mueller scanning microscopy," *Biomed. Opt. Express* **12**, 41–54 (2021).
5. M. Menzel et al., "Diattenuation imaging reveals different brain tissue properties," *Sci. Rep.* **9**, 1939 (2019).
6. G. Agnoil et al., "Ship detection performance using simulated dual-polarization RADARSAT constellation mission data," *Int. J. Remote Sens.* **36**, 1705–1727 (2015).
7. Y. Wang et al., "Assessment of system polarization quality for polarimetric SAR imagery and target decomposition," *IEEE Trans. Geosci. Remote Sens.* **49**, 1755–1771 (2011).
8. M. Karouzos, "Cloudy with a chance of depolarization," *Nat. Astron.* **5**, 224 (2021).
9. A. Van Eeckhout et al., "Depolarizing metrics for plant samples imaging," *PLoS One* **14**, e0213909 (2019).
10. A. Van Eeckhout et al., "Polarimetric imaging of biological tissues based on the indices of polarimetric purity," *J. Biophotonics* **11**, e201700189 (2018).
11. X. Li et al., "Near-infrared monocular 3D computational polarization imaging of surfaces exhibiting nonuniform reflectance," *Opt. Express* **29**, 15616–15630 (2021).
12. M. Ballesta-Garcia et al., "Analysis of the performance of a polarized LiDAR imager in fog," *Opt. Express* **30**, 41524–41540 (2022).
13. I. Estévez et al., "Urban objects classification using Mueller matrix polarimetry and machine learning," *Opt. Express* **30**, 28385–28400 (2022).
14. R. Maldzius, T. Lozovski, and J. Sidaravicius, "Influence of environmental relative humidity on the polarization behaviour of paper and paper-dielectric structures," *Cellulose* **27**, 10303–10312 (2020).
15. A. Lizana et al., "Enhanced sensitivity to dielectric function and thickness of absorbing thin films by combining total internal reflection ellipsometry with standard ellipsometry and reflectometry," *J. Phys. D: Appl. Phys.* **46**, 105501 (2013).
16. D. Li et al., "Polarization characteristics motivating target detection in different polarization spaces," *Opt. Laser Technol.* **171**, 110430 (2024).
17. D. Li et al., "Depolarization characteristics of different reflective interfaces indicated by indices of polarimetric purity (IPPs)," *Sensors* **21**, 1221 (2021).
18. D. Li et al., "Measuring glucose concentration in a solution based on the indices of polarimetric purity," *Biomed. Opt. Express* **12**, 2447–2459 (2021).

19. D. Ivanov et al., "Polarization and depolarization metrics as optical markers in support to histopathology of ex vivo colon tissue," *Biomed. Opt. Express* **12**, 4560–4572 (2021).
20. C. Rodríguez et al., "Automatic pseudo-coloring approaches to improve visual perception and contrast in polarimetric images of biological tissues," *Sci. Rep.* **12**, 18479 (2022).
21. A. Pierangelo et al., "Ex vivo characterization of human colon cancer by Mueller polarimetric imaging," *Opt. Express* **19**, 1582 (2011).
22. E. Du et al., "Mueller matrix polarimetry for differentiating characteristic features of cancerous tissues," *J. Biomed. Opt.* **19**, 076013 (2014).
23. C. Rodríguez et al., "Polarimetric data-based model for tissue recognition," *Biomed. Opt. Express* **12**, 4852 (2021).
24. Y. Xu et al., "Spin-decoupled multifunctional metasurface for asymmetric polarization generation," *ACS Photonics* **6**, 2933–2941 (2019).
25. T. Huang et al., "Polarization-decoupled cavity solitons generation in Kerr resonators with flattened near-zero dispersion," *Opt. Express* **30**, 20767–20782 (2022).
26. K. Luo et al., "Study of polarization transmission characteristics in nonspherical media," *Opt. Lasers Eng.* **174**, 107970 (2024).
27. Q. Xu et al., "Transmitting characteristics of the polarization information under seawater," *Appl. Opt.* **54**, 6584–6588 (2015).
28. F. Shen et al., "The depolarization performances of the polarized light in different scattering media systems," *IEEE Photonics J.* **10**, 3900212 (2018).
29. S. Miao et al., "Image denoising and enhancement strategy based on polarization detection of space targets," *Appl. Opt.* **61**, 904–918 (2022).
30. B. Yang et al., "Tunable circular polarization detection and full stokes measurement structure," *IEEE Photonics J.* **13**, 5800109 (2021).
31. L. Qu and H. Kim, "A novel single-feed dual-element antenna using phase compensation and magnitude regulation to achieve circular polarization," *IEEE Trans. Antennas Propag.* **66**, 5098–5108 (2018).
32. Y. Cai et al., "Compact, high-performance all-polarization-maintaining Er: fiber frequency comb with single fiber actuator," *IEEE Photonics J.* **12**, 7102508 (2020).
33. X. Wang et al., "Performances of polarization-retrieve imaging in stratified dispersion media," *Remote Sens.* **12**, 2895 (2020).
34. P. Wang et al., "Analyzing polarization transmission characteristics in foggy environments based on the indices of polarimetric purity," *IEEE Access* **8**, 227703–227709 (2020).
35. A. Eeckhout et al., "Depolarization metric spaces for biological tissues classification," *J. Biophotonics* **13**, e202000083 (2020).
36. A. Van Eeckhout et al., "Unraveling the physical information of depolarizers," *Opt. Express* **29**, 38811–38823 (2021).
37. J. J. Gil, "Components of purity of a three-dimensional polarization state," *J. Opt. Soc. Am. A* **33**, 40 (2016).
38. H. Hu et al., "Polarimetric image recovery in turbid media employing circularly polarized light," *Opt. Express* **26**, 151–155 (2018).
39. J. Liang et al., "Visibility enhancement of hazy images based on a universal polarimetric imaging method," *J. Appl. Phys.* **116**, 173107–173113 (2014).
40. J. J. Gil and R. Ossikovski, *Polarized Light and the Mueller Matrix Approach*, CRC Press (2022).
41. R. Huynh, G. Nehmetallah, and C. Raub, "Mueller matrix polarimetry and polar decomposition of articular cartilage imaged in reflectance," *Biomed. Opt. Express* **12**, 5160–5178 (2021).
42. R. Ossikovski, "Canonical forms of depolarizing Mueller matrices," *J. Opt. Soc. Am. A* **27**, 123–130 (2010).
43. V. Albert et al., "Synthesis and characterization of depolarizing samples based on the indices of polarimetric purity," *Opt. Lett.* **42**, 4155–4158 (2017).
44. J. J. Gil, "Transmittance constraints in serial decompositions of depolarizing Mueller matrices. The arrow form of a Mueller matrix," *J. Opt. Soc. Am. A* **30**, 701–707 (2013).
45. S. Lu and R. Chipman, "Interpretation of Mueller matrices based on polar decomposition," *J. Opt. Soc. Am. A* **13**, 1106–1113 (1996).
46. A. Tariq et al., "Purity-depolarization relations and the components of purity of a Mueller matrix," *Opt. Express* **27**, 22645–22662 (2019).
47. D. Li et al., "High-performance scanning-mode polarization based computational ghost imaging (SPCGI)," *Opt. Express* **30**, 17909–17921 (2022).
48. D. Li et al., "High-performance polarization remote sensing with the modified U-Net based deep-learning network," *IEEE Trans. Geosci. Remote Sens.* **60**, 5621110 (2022).
49. R. Ossikovski and J. Vizet, "Eigenvalue-based depolarization metric spaces for Mueller matrices," *J. Opt. Soc. Am. A* **36**, 1173–1186 (2019).
50. A. Tariq et al., "Physically realizable space for the purity-depolarization plane for polarized light scattering media," *Phys. Rev. Lett.* **119**, 033202 (2017).
51. C. He et al., "Revealing complex optical phenomena through vectorial metrics," *Adv. Photonics* **4**, 026001 (2022).
52. A. Aiello and J. Woerdman, "Physical bounds to the entropy-depolarization relation in random light scattering," *Phys. Rev. Lett.* **94**, 090406 (2005).
53. F. Shen et al., "The depolarization performances of scattering systems based on the indices of polarimetric purity (IPPs)," *Opt. Express* **27**, 28337–28349 (2019).
54. D. Li, "Polarizance-reflection-transformation representation space for sensing and distinguishing pure systems," *IEEE Sens. J.* **24**, 14763–14769 (2024).
55. M. Canabal-Carbia et al., "Connecting the microscopic depolarizing origin of samples with macroscopic measures of the indices of polarimetric purity," *Opt. Lasers Eng.* **172**, 107830 (2024).
56. R. Ossikovski, A. Martino, and S. Guyot, "Forward and reverse product decompositions of depolarizing Mueller matrices," *Opt. Lett.* **32**, 689–691 (2007).
57. R. Ossikovski, "Analysis of depolarizing Mueller matrices through a symmetric decomposition," *J. Opt. Soc. Am. A* **26**, 1109–1118 (2009).

Dekui Li received his BE degree in software engineering from the Henan Polytechnic University in 2019. He received his PhD from the Hefei University of Technology in 2024. He was a joint PhD student at the Autonomous University of Barcelona from 2023 to 2024, supported by China Scholarship Council. His research interests include polarization imaging, polarization representation, and polarization information processing.

Ivan Montes-Gonzalez received his BSc degree in physics from the Universidad Nacional Autónoma de México (UNAM) and his ME and PhD degrees in optical engineering from ICAT, UNAM. His research focuses on characterizing liquid crystals and developing Stokes and Mueller polarimeters. Currently, he is a postdoc at the Autonomous University of Barcelona, working on imaging polarimeters for biomedical diagnosis, particularly for skin pathologies. His interests include polarimetric systems for biological samples and studying anti-cancer compounds in preclinical models.

Mónica Canabal Carbia received her BSc degree in physics at the University of Santiago de Compostela (USC) in 2020 and her MSc degree in physics of light and radiation at the USC in 2021. Her current thesis topic in UAB is framed in the field of polarization, studying the polarimetric response of biological tissue in light–matter interaction processes and developing polarimetric instrumentation and methods to be used in biomedical and botanical applications.

Irene Estévez received her PhD in physics from the Universitat Autònoma de Barcelona in 2018, receiving her PhD Extraordinary

Award. She has been a visiting scholar at the École Polytechnique and a postdoc at the CFUMP, collaborating with BOSCH. In 2023, she was a Beatriu de Pinós fellow. Her research focuses on polarimetry, optical design, and polarized light applications. She has 15 peer-reviewed articles, 3 patents, and has presented at major conferences.

Octavi López began his research in 1996 at the Autonomous University of Barcelona (UAB), specializing in spatial light modulators and diffractive optics. He earned his PhD in 2007 with a thesis on non-uniform transmission pupils and multiplexed lenses. He has been an adjunct professor at UPC and UAB since 2000. He combines teaching and research in optics with work in scientific communication at UAB's Communication Unit.

Zhongyi Guo received his BSc degree and PhD from the Department of Physics, Harbin Institute of Technology in 2003 and 2008, respectively. He held postdoctoral positions with the Hanyang University and Hong Kong Polytechnic University, respectively. Then, he joined the Hefei University of Technology as a full professor at the end of 2011. His research interests mainly include advanced optical communication, OAM antenna, polarization information processing, manipulation of optical fields, and nanophotonics

Juan Campos has worked in optical image system quality, optical pattern recognition, diffractive optics, and metrology. His contributions include the design of non-uniform pupils, apodizers in photolithography, liquid crystal spatial light modulators, optical pattern recognition with color information, numerical methods in deflectometry and interferometry, and Stokes and Mueller polarimeters. He has published over 270 papers, 3 book chapters, and presented more than 250 conference communications.

Ángel Lizana received his MSc degree and PhD in physics from the Universitat Autònoma de Barcelona in 2006 and 2011, respectively. His research focuses on liquid crystal displays, diffractive optics, and polarimeters, including polarimetric methods for biological tissues. He has been a postdoc at the École Polytechnique, optimizing infrared polarimeters. He has published over 70 papers, 2 book chapters, and presented 80+ conference communications. He was SEDOPTICA's secretary general (from 2019 to 2023).